

A comparison of the neutron detection efficiency and response characteristics of two pixelated PSD-capable organic scintillator detectors with different photo-detection readout methods

J. Balajthy^{a,1} P. Marleau^a M. Sweany^a

^a*Sandia National Laboratory, Livermore, CA 94550, USA*

E-mail: jabalaj@sandia.gov

ABSTRACT: We characterize the performance of two pixelated neutron detectors: a PMT-based array that utilizes Anger logic for pixel identification and a SiPM-based array that employs individual pixel readout. The SiPM-based array offers improved performance over the previously developed PMT-based detector both in terms of uniformity and neutron detection efficiency. Each detector array uses PSD-capable plastic scintillator as a detection medium. We describe the calibration and neutron efficiency measurement of both detectors using a ^{137}Cs source for energy calibration and a ^{252}Cf source for calibration of the neutron response. We find that the intrinsic neutron detection efficiency of the SiPM-based array is $(30.2 \pm 1.7)\%$, which is almost twice that of the PMT-based array, which we measure to be $(16.9 \pm 0.2)\%$.

KEYWORDS: Front-end electronics for detector readout, Neutron detectors, Neutron Imaging

¹Corresponding author.

Contents

1	Introduction	1
2	Experimental Setup	2
3	Data Processing and Calibration	4
3.1	PMT-based Detector Processing	4
3.2	SiPM-Based Detector Processing	6
3.3	Energy	8
3.4	Pulse Shape Discrimination	10
4	Neutron Detection Efficiency	13
5	Conclusion	18
6	Acknowledgments	19

1 Introduction

Enabling a fieldable pixelated fast neutron detection or imaging plane has many challenges, including maximizing the neutron detection efficiency while minimizing size, weight, and power (SWaP). Some current and widely used fast neutron detection systems minimize the number of readout channels, and thus system complexity and power requirements, by employing Anger logic readout using photomultiplier tubes [1]. However, this leads to poor light collection efficiency for certain pixels and does not allow for multiple interactions from the same neutron to be resolved, which reduces the intrinsic neutron detection efficiency [2]. Advances in Silicon Photomultiplier (SiPM) technology makes highly pixelated photo-detection with $O(100)$ ps timing feasible, allowing for cost effective independent readout of scintillator pixels and the ability to resolve multiple fast neutron scatters in the same volume that occur within less than 1 ns. Furthermore, the improved photo-detection efficiency of SiPMs compared to PMTs [3–5] coupled with light collection efficiency improvements from 1-to-1 scintillator/photodetector coupling has the potential to greatly improve the intrinsic neutron detection efficiency. SiPMs are also lighter, more compact, and require less power than PMTs. Provided enough investment into low power, high channel acquisition using either FPGA-based methods (see e.g. [6–8]) or ASICs, a pixelated fast neutron detection plane with SiPM-based readout of each scintillator pixel may approach the necessary efficiency and SWaP requirements for fieldable systems.

Here, we quantify the intrinsic neutron detection efficiency of two pixelated neutron detectors: one 10x10 pixelated array read out with four PMTs via Anger logic, and one 8x8 pixelated array individually read out with a commercial 8x8 SiPM array. The two detectors differ slightly in

scintillator composition, however the largest differences are the size and number of scintillator pixels and how they are read out. We use the nomenclature "PMT-based" and "SiPM-based" to distinguish between the two. Both scintillator arrays are manufactured by Agile Technologies. Section 2 describes the two detectors, and also details the measurement setup used to characterize them. Section 3 presents the calibration and response of each detector. Finally, the intrinsic neutron detection efficiency results are presented in Section 4.

2 Experimental Setup

The PMT-based detector consists of one hundred 1.08 cm x 1.08 cm x 5 cm pixels of pulse shape discrimination (PSD)-capable plastic scintillator EJ299-34. Each scintillator pixel is individually wrapped with a layer of 3M's Enhanced Specular Reflector (ESR) material. The 10x10 pixelated scintillator array is read out by four Hamamatsu R7724-100 super bialkali photomultiplier tubes, and Anger logic is used to determine which pixel a scintillation event occurred in. An acrylic (PMMA) light guide couples the scintillator array to the four PMTs. The detectors also include a layer of $^6\text{Li}/\text{ZnS:Ag}$ for thermal neutron detection. ZnS:Ag has a phosphorescence response to the particles (α, t) released by neutron capture on ^6Li . Because of its comparatively long decay time, phosphorescence is easily distinguished from scintillation in EJ-299-34 by PSD. A photograph of a single detector is shown in Figure 1. The performance of the PMT-based detectors has been characterized in previous work [2, 9], however in order to provide a comparison with the SiPM-based detector using the same characterization procedures, much of the characterization is repeated here.

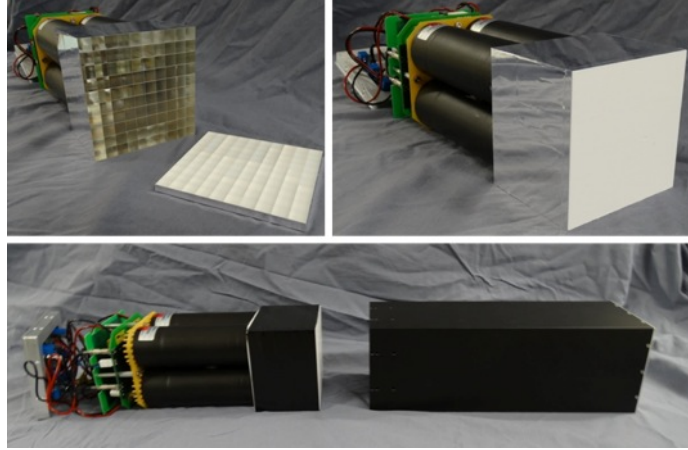


Figure 1. Images of the PMT-based detector, courtesy P. A. Hausladen of Oak Ridge National Laboratory.

The SiPM-based detector is an 8x8 array of EJ-299-33M PSD-capable plastic scintillator, and is shown in Figure 2a, b. The scintillator pixel size and pitch are designed to match the SiPM array ArrayJ-60035-64P-PCB from SensL/onsemi, which has 6.13 mm x 6.13 mm SiPMs with a pitch of 6.33 mm mounted on a printed circuit board (PCB). The scintillator pixels are 5 cm long. Between each scintillator pixel are two layers of 3M's ESR and one layer of Aluminum between the two ESR layers. ESR is also layered on the front side of the array, which does not include $^6\text{Li}/\text{ZnS:Ag}$. The

scintillator array is coupled with silicon-based optical grease directly to the SiPM array without a light guide. The SiPM array is mated to a custom 64 channel breakout board, shown in Figure 2c, that is based on the readout circuit described in [10]. The board is biased at (-)30 V with a B&K Precision 1761 DC power supply. The standard outputs of the SiPM pixels are coupled in groups of 16 with header pins that mate to CAEN’s A385 adaptor with MCX connectors. The assembly is housed in a light tight enclosure.

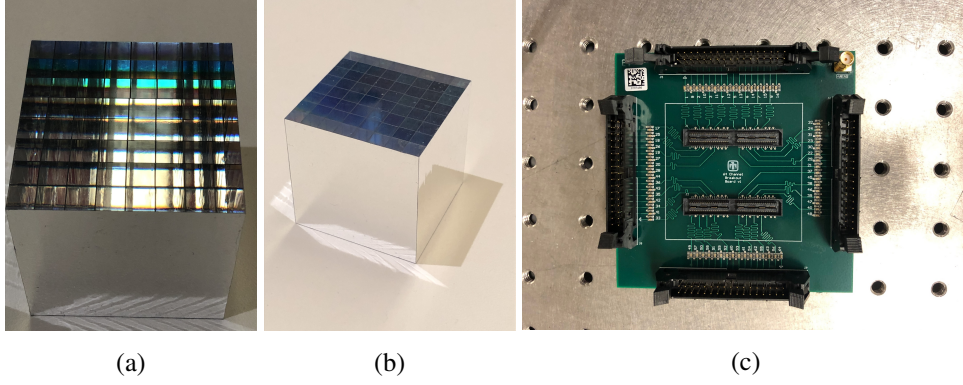


Figure 2. The SiPM-based scintillator array (a and b), and the custom SiPM readout board (c).

A ^{137}Cs source is used for energy calibration for both the PMT-based detector and the SiPM-based detector. The ^{137}Cs source is positioned such that it is approximately centered with respect to the face of the detector array, at a distance such that the rate is maximized without overwhelming the data acquisition (DAQ). This is approximately 40 cm for the PMT-based detector, and 10 cm for the SiPM-based array.

A single ^{252}Cf measurement for each of the detectors is used for both the PSD calibration and neutron efficiency measurement. For each of the measurements, the ^{252}Cf source is positioned so that it is centered to within 1 cm with respect to the face of the detector. For the PMT-based detector measurements, the source is placed at a distance of 142.0 ± 0.3 cm from the face of the detector, and for the SiPM-based measurement, the source is placed at 40.0 ± 0.3 cm from the face of the detector.

Each PMT anode output is passed through an integrating preamplifier [9] before being digitized using a CAEN DT5730s desktop digitizer with DPP_PSD firmware [11]. The digitizer samples at rate of 500 MHz and is operated with a 2V vertical scale. The waveforms from the PMTs are acquired using the CoMPASS data acquisition software from CAEN [12]. The local triggers for each PMT channel are configured in the leading edge mode. The digitizer is configured so that a local trigger from any of the four PMT channels will initiate a global trigger, and all four PMT channels are read out simultaneously on any global trigger. There are a small number of events ($<0.04\%$) in which the waveforms for individual channels have been lost, likely due to pileup. This number of events will be negligible for our efficiency calculations in Section 4.

Waveforms from the 64-channel SiPM array are digitized using four CAEN v1725 digitizers with DPP_PSD firmware, and installed in a VME crate [13]. The v1725 digitizers have a sample rate of 250 MHz and are operated with a 500 mV full-scale and a 5% DC offset. The CoMPASS software from CAEN is again used for waveform acquisition. We configure the digitizers to acquire

asynchronously, allowing each channel to trigger independently. The channel triggers are all configured in “CFD” mode, with a 28 ns CFD delay and a 50% CFD fraction. The CFD threshold is set to 110 lsb for most channels, or roughly 0.050 MeVee for neutrons. Several channels are observed to have excess electronic noise, and their thresholds were set higher. No triggers were reported as being lost by the CoMPASS software in the SiPM-based ^{137}Cs and ^{252}Cf measurements.

3 Data Processing and Calibration

Data processing and calibration operations are mostly written in C++, utilizing algorithms from the ROOT analysis toolkit [14]. Some high-level analysis is performed in Python, including the time offset calibration shown in Figure 5 and the neutron efficiency calculations described in Section 4. The Python packages we use most heavily are NumPy[15], SciPy[16], Matplotlib[17], and upRoot[18]. Digital waveform processing is applied to pulses from both the PMT-based and SiPM-based detectors and are then organized by time and pixel number. The processed pulse values are then calibrated for energy and PSD. The calibrated data is used in Section 4 for the neutron efficiency calculation.

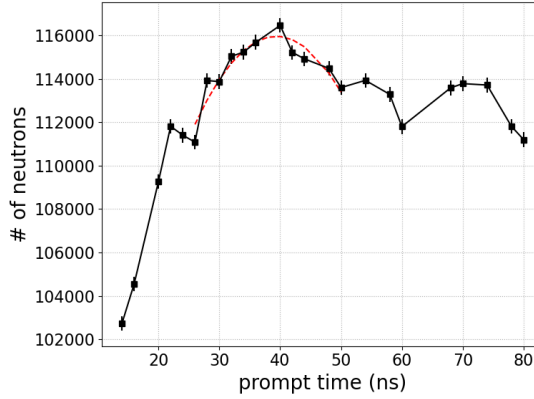


Figure 3. Optimization for prompt gate time in the PMT-based detector. The black markers show the number of observed neutrons as a function of prompt gate time. The red dashed line shows a quadratic fit to these results. Results are calculated using about 10% of the entries in the ^{252}Cf dataset.

3.1 PMT-based Detector Processing

Waveforms from the four channels of the PMT-based detector are baseline-subtracted using samples 10 through 60 and are then sorted and matched according to the fine timestamp reported by the digitizer. For a given interaction, the four matched waveforms are summed together in software, and the summed waveform is smoothed using a 5-bin centered moving average filter. The pulse time relative to the trigger window is taken to be the linearly interpolated value between samples in the summed and smoothed waveform corresponding to 50% of the maximum value on the rising edge. The individual PMT waveforms are smoothed using the same 5-bin centered moving average filter, are baseline-subtracted, and then are linearly interpolated at $t = 40$ ns and $t = 832$ ns relative to the pulse time. These values are stored for all four PMTs as the prompt and total pulse amplitudes,

respectively (A_p and A_t). A gate time of 832 ns for A_t has been previously identified as yielding optimal energy results [2, 9]. We optimize the gate time for A_p using approximately the first 10% of entries in the ^{252}Cf . We process this subset of data multiple times, using a different prompt gate time for each iteration. We calculate the number of observed neutrons for each processing as described in Section 4, and fit a quadratic polynomial to the values around the maximum, as is shown in Figure 3. The optimal prompt gate time is taken to be the maximum value of the quadratic fit.

The ^{252}Cf measurement for the PMT-based detector is used to generate a look up table to identify the pixel number from the x -position and y -position measures from Anger logic:

$$x_i = \frac{A_{2,i} + A_{3,i}}{\sum_{p=0}^3 A_{p,i}}, \text{ and } y_i = \frac{A_{0,i} + A_{2,i}}{\sum_{p=0}^3 A_{p,i}} \quad (3.1)$$

For the i^{th} entry in a measurement, $A_{p,i}$ is the “total” pulse integral value observed by the PMT with index p . The uppermost PMTs have indices $p = 0$ and $p = 2$, while the leftward most PMTs have indices $p = 2$ and $p = 3$. The software for the implementation of the look up table algorithm was developed by M. A. Blackston and R. J. Newby of Oak Ridge National Laboratory. The algorithm seeds 100 2-D Gaussian fits based on local maxima with an assumed standard deviation for each pixel. The cell boundaries are determined based on where neighboring pixels’ responses are equalized. A human user checks and refines the result if necessary. The measured Anger logic lookup table is shown in Figure 4.

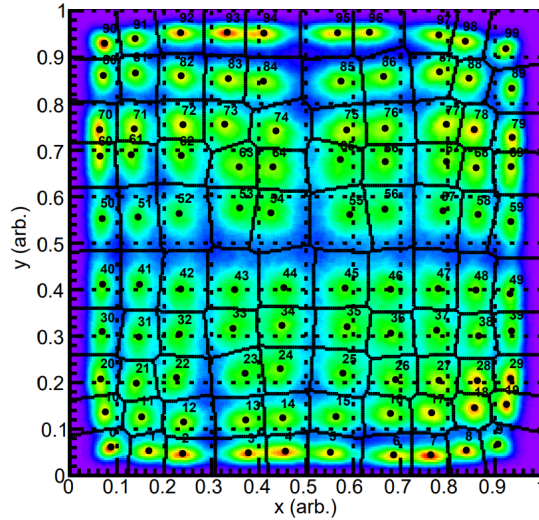


Figure 4. Anger logic look-up table for the PMT-based detector, measured using the ^{252}Cf . The values of x and y are values of the Anger logic x and y described in the text. The solid black lines show the divisions between the detector pixels, and the dashed lines show a uniform 10x10 grid. The numbered markers indicate the peak position for each of the 100 detector pixels.

3.2 SiPM-Based Detector Processing

The waveforms from the SiPM-based detector are baseline subtracted using the first 80 ns of the trace and a centered moving average filter is applied. The cumulative distribution of the baseline-subtracted waveform is used to calculate the pulse integral for total energy deposition measurements. The integral is evaluated exactly 280 ns after the measured pulse time using a linear interpolation of the cumulative distribution of the waveform. The pulse time is the linearly interpolated value between waveform samples corresponding to 50% of the maximum value on the rising edge. For pulse shape measurements on the SiPM-based detector, we linearly interpolate between samples of the cumulative distribution of the waveform for the value corresponding to the desired integration window.

The fine timestamp reported by the CAEN digitizers is used for the trigger time of each interaction. Time offsets between the four v1725 boards are measured using ^{22}Na coincident interactions. Two 6 mm x 6mm x 6mm *trans*-Stilbene crystals are coupled to SiPM pixels that are read out by neighboring digitizer boards, and the ^{22}Na source is placed directly between the two. The time difference spectrum is measured for each of the three selected channel pairs (15 and 16, 31 and 32, and 47 and 48), and the coincidence peak is identified. We use only events with pulse heights between 150 and 350 mV for our coincidence analysis. The location of the ^{22}Na Compton edge ranges from 254 to 290 mV for the six pixels tested, so the pulse height selection cut corresponds to roughly 190 keVee to 450 keVee. The Gaussian mean and width of each coincidence peak is shown in Figure 5. We measure a coincident timing resolution of about 300 ps for each channel pair. The interaction timestamps for the ^{137}Cs and ^{252}Cf datasets are adjusted according to the mean values of the ^{22}Na coincident peaks. We will refer to the adjusted fine time stamp for interaction i in a given dataset as T_i .

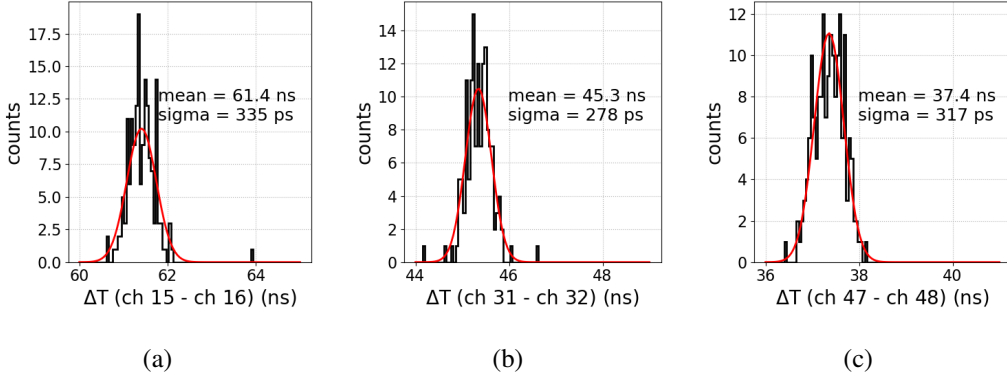


Figure 5. Coincidence peaks for ^{22}Na calibration of SiPM array timing offsets. Plot (a) shows the time differences for digitizer boards 0 and 1, (b) shows the time differences for boards 1 and 2, and (c) shows the time differences for boards 2 and 3.

A coincidence rejection processing step is added for the SiPM-based ^{137}Cs and ^{252}Cf datasets. This primarily rejects pulses caused by light sharing between detector pixels and pulses due to multiple scattering interactions in adjacent pixels by the same particle. This also removes accidental coincidences from our dataset, which is expected to be small compared to light sharing and multi scatter events.

We identify “events” of coincident pulses by looping across all trigger times in a dataset. A pair of consecutive pulses, i and $i + 1$, is considered coincident and both are elements of the same event, N , if $T_{i+1} - T_i < 50$ ns. In the case that $T_{i+2} - T_{i+1}$ is also < 50 ns, then pulse $i + 2$ will also be included in event N . Subsequent pulses are added to event N until a pair of non-coincident pulses is found. If a pulse i is coincident with neither $i + 1$ or $i - 1$, it will be assigned to its own event with only one pulse. Events will therefore range in size from a single pulse to an arbitrary number of coincident pulses. For each event we label the pulse with largest integral value as the “primary” interaction, and we label the rest of the pulses in the event as “coincidence” interactions. We expect this to be sufficient for neutron efficiency measurements, as the order of pulses in an event is not important, however a more careful treatment is required for neutron imaging to identify the pixel location of the first pulse in a chain. The set of pulses identified as primary interactions are used for the energy calibration, PSD calibration, and neutron detection efficiency calculations.

We select a time difference threshold of 50 ns in order to reject all the excess low-time difference pulses seen in the coincidence histograms shown in Figure 6. There are two peaks below 10 ns time difference observed in both the ^{137}Cs and ^{252}Cf coincidence histograms which we identify as coming primarily from light sharing. We have found that the second of these peaks is due to a mis-calibration in the timing offset for the fourth board, likely caused by excess electronic noise, that causes an 8 ns shift in trigger times relative to other boards. This shift is well under our 50 ns threshold, so we do not expect it to significantly impact our coincidence rejection. There is a third, broader peak that is observed only in the ^{252}Cf histogram that ends at about 50 ns time difference that we attribute to multiple scatters of fast neutrons.

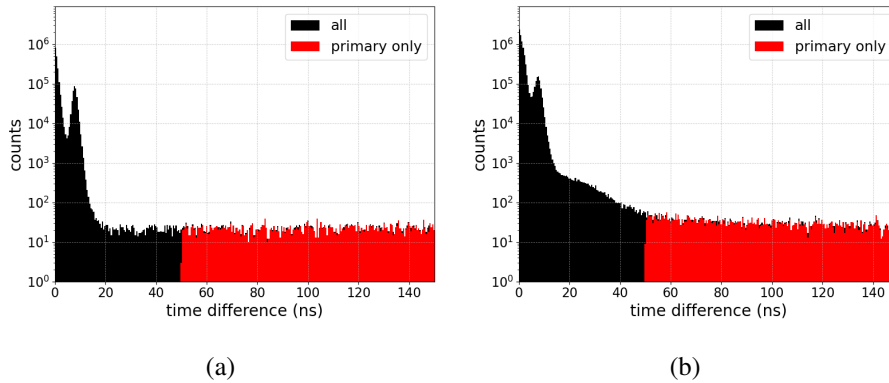


Figure 6. Histograms of time differences between consecutive interactions for the SiPM-based ^{137}Cs (left) and ^{252}Cf datasets (right). The black histograms contain all interactions in the datasets, while the red histograms contain only interactions identified as “primary” by the coincidence rejection described in the text.

The effects of the coincidence rejection on the pulse integral spectra for the the ^{137}Cs and ^{252}Cf datasets are shown in Figure 7. The “primary” only selections show a significant reduction at low pulse integrals. The Compton edge of the ^{137}Cs spectrum appears to be well preserved, and the shape of the ^{252}Cf spectrum above ADC channel 2500 is largely unaffected. The coincidence rejection removes 14.9% of events from the ^{137}Cs dataset and 24.4% of events from the ^{252}Cf dataset.

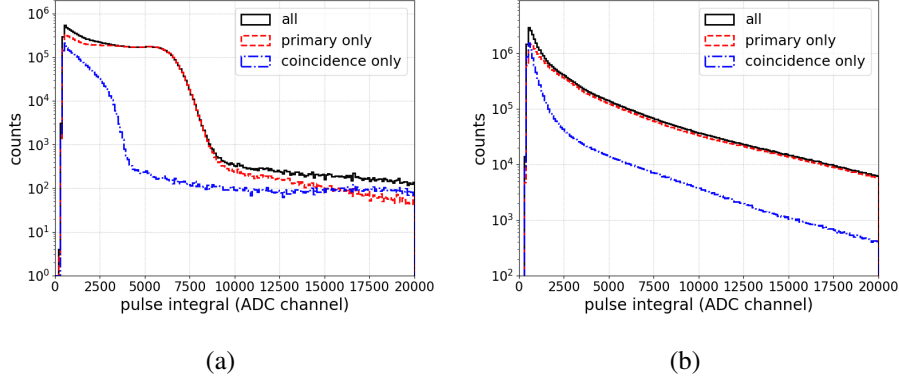


Figure 7. Histograms of pulse integrals for the SiPM-based ^{137}Cs (left) and ^{252}Cf datasets (right). The black histograms contain all events in the datasets, the red histograms contain only events identified as “primary” by the coincidence rejection described in the text, and the blue histograms contain only events labeled “coincidence”.

3.3 Energy

The calibration from pulse integral to MeVee is determined by fitting the measured spectrum from a ^{137}Cs source to a Klein-Nishina convolved with an energy-dependent Gaussian [19]. The method is similar to that described in [20]. The pulse integral spectrum from the ^{137}Cs source is used to compare to the expected spectrum calculated from the Klein-Nishina prediction. First, the experimental result is converted to MeVee units with a linear transformation:

$$E_{\text{MeVee}} = q_0 E_{\text{mV}}. \quad (3.2)$$

Next, an arbitrary y-scale, q_1 , is applied to the Klein-Nishina prediction for the gamma emissions, and a Gaussian convolution is performed with a standard deviation of:

$$\sigma = q_2 E_{\text{MeVee}}. \quad (3.3)$$

The fit region is restricted to a range near the Compton edge. In this case, the primary parameter of interest is the conversion factor to MeVee. Figure 8 shows an example fit for one pixel of the SiPM-based detector.

The energy spectra for the calibrated ^{137}Cs datasets measured by the PMT-based detector and SiPM-based array are shown in Figures 9 and 10, respectively. In Figure 11 we compare the integrated light collection observed by the two detectors for events with calibrated energy from 0.472-0.482 MeVee. The total pulse amplitude converted in mV is used as the measure of light collection for the PMT-based detector, and the pulse integral in mV·ns is used for the SiPM-based array. The histograms in Figure 11 contain pulse information from all the pixels in the respective detectors. The reported light collection is 63 ± 13 mV for the PMT-based detector and 770 ± 54 mV·ns for the SiPM-based array. The error reported is the standard deviation of the projected distribution. We find that our energy calibration performed as expected for both systems, and that the response of the SiPM-based array is significantly more uniform across detector pixels.

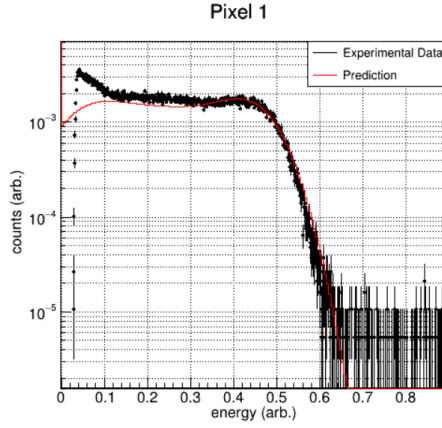


Figure 8. An example Compton edge fit, with the smeared Klein-Nishina spectrum from ^{137}Cs shown in red, and the experimental data in black.

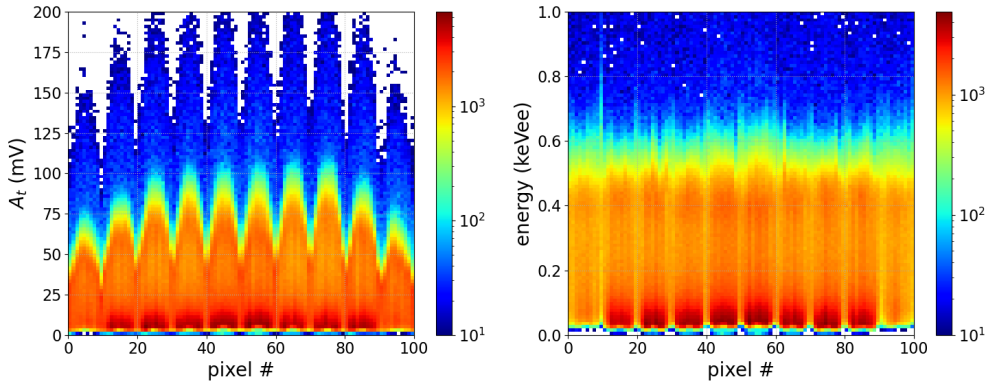


Figure 9. This figure shows the energy response of the PMT-based detector to the ^{137}Cs calibration. The left panel shows the pulse integral measure (A_{total}) for each pixel in the PMT-based detector. The right panel shows the calibrated energy for each pixel in the PMT-based detector.

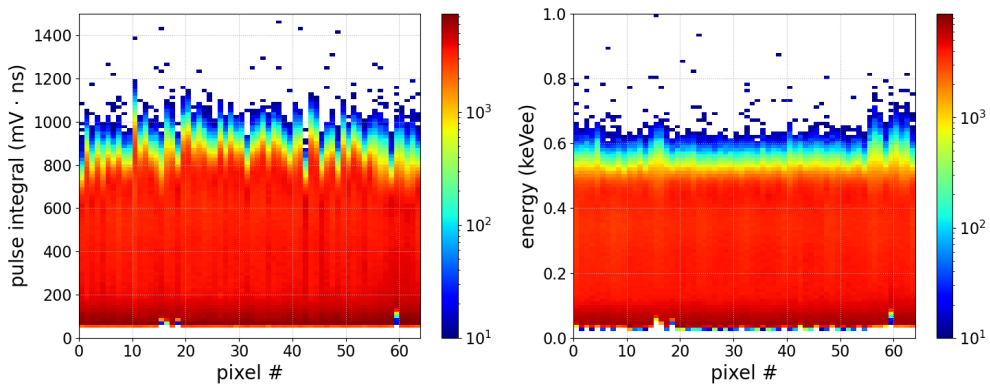


Figure 10. This figure shows the energy response of the SiPM-based array to the ^{137}Cs calibration. The left panel shows the pulse integral measure (A_{total}) for each pixel in the array. The right panel shows the calibrated energy for each pixel in the array.

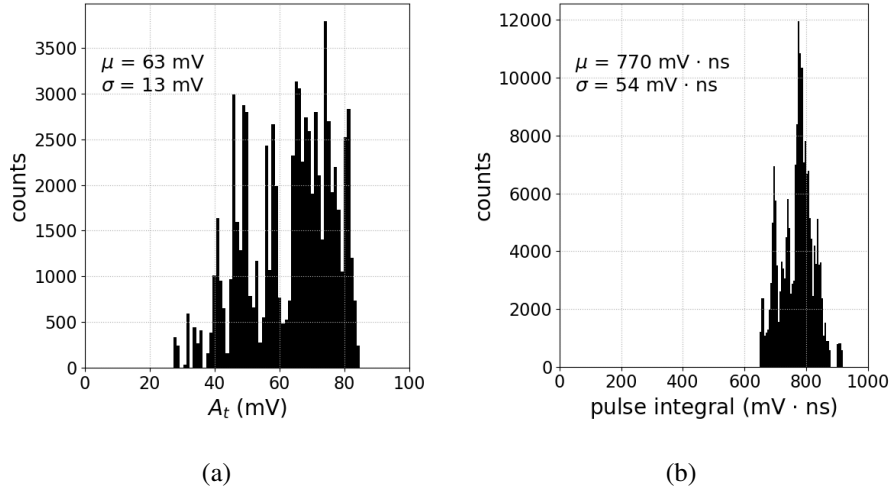


Figure 11. This figure compares the light collection uniformity for the PMT-based detector (a) with the SiPM-based array (b). The both plots include pulses with calibrated energy between 0.472-0.482 MeV from all pixels in the histograms. The PMT-based detector plot uses the total amplitude, converted to mV as the measure of light collection, and the SiPM-based array plot uses pulse integral value in mV·ns.

3.4 Pulse Shape Discrimination

For the PMT-based detector, the PSD values for the four PMTs are given by the prompt amplitude for the given PMT waveform (A_p), divided by the total amplitude (A_t). The PSD measured by each PMT will be used in Section 4 to select a neutron population. The PSD calculated using the sum of the four PMT pulses will be used for visualization purposes only. Figure 12 shows the measured PSD as a function of A_t for each of the four PMTs in the PMT-based detector. For each PMT, we bin the ^{252}Cf dataset into 10-ADC wide increments of A_t . We combine consecutive increments until at least 5,000 entries are included and then apply double Gaussian fits to the PSD projection in the selected increments. This fitting procedure is repeated across the entire range in order to find A_t -dependent means and standard deviations of the gamma and neutron bands, which are taken from the double Gaussian fits. We then fit simple functional forms to the measured means and standard deviations:

$$\mu_\gamma(A_t) = a + bA_t \quad (3.4)$$

$$\mu_N(A_t) = a + b \exp cA_t \quad (3.5)$$

$$\sigma_{\gamma,N}(A_t) = a + \frac{b}{A_t} + \frac{c}{A_t^2}. \quad (3.6)$$

$$(3.7)$$

The best fit functions are shown in Figure 12 and are used to calculate the gamma and neutron probabilities described in Section 4.

For the SiPM-based array, we characterize the PSD using the ratio of the prompt pulse integral to the total pulse integral. The end time of the prompt region is determined by optimizing the figure-of-merit, defined as

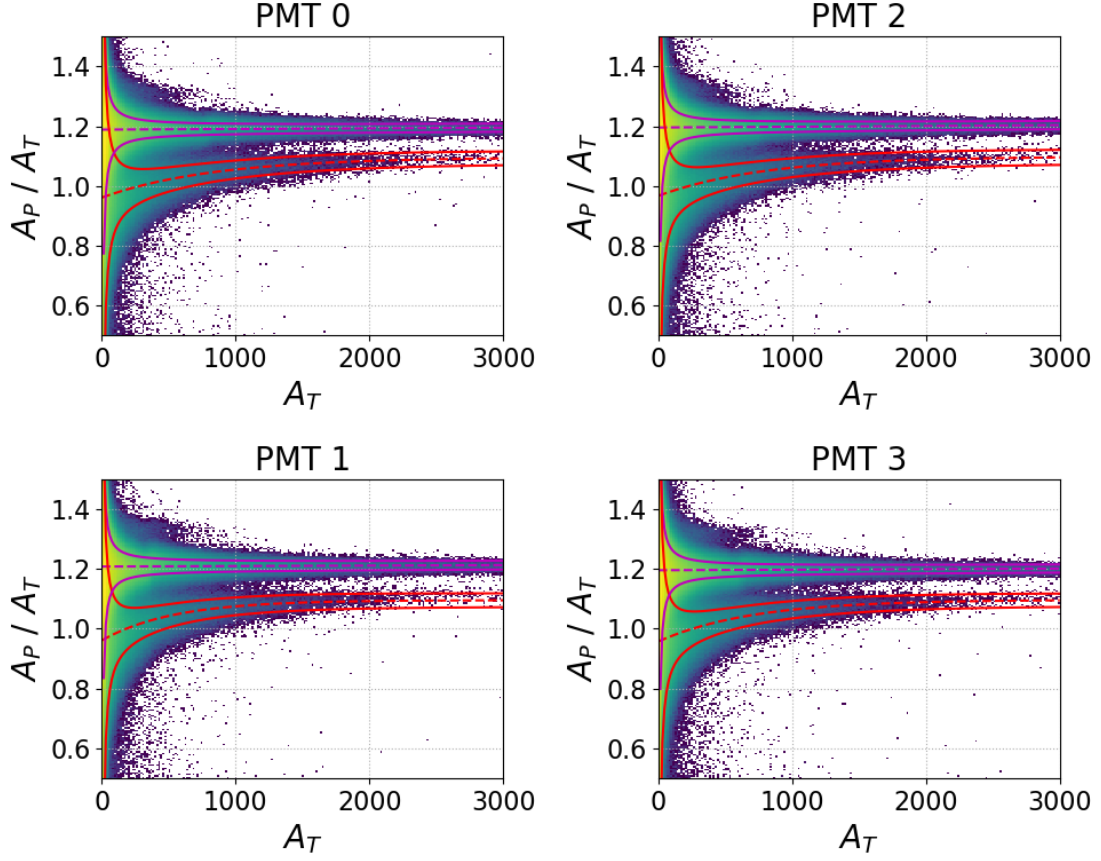


Figure 12. Measured histograms of PSD versus total amplitude value for the four detector PMTs. The dashed and solid lines show the best fit functions (Equations 3.4 to 3.6) for the means and standard deviations of the gamma (magenta) and neutron (red) bands.

$$FoM = \frac{\mu_n - \mu_\gamma}{2.355(\sigma_n + \sigma_\gamma)}, \quad (3.8)$$

where $\mu_{n/\gamma}$ is the mean of a Gaussian fit to the neutron and gamma distributions, $\sigma_{n/\gamma}$ is the standard deviation of the Gaussian fit, and the factor of 2.355 is for conversion to a FWHM width. The shape of the fission neutron energy spectrum favors optimizing the FoM for lower energy depositions in order to maximize overall neutron detection efficiency.

We scan across prompt end times to identify the value that optimizes the PSD FoM for the SiPM-based array. For each prompt end time selection, we evaluate linear interpolations of the calculated FoM for each pixel in the detector at 0.2 MeVee, 0.34 MeVee, and 1 MeVee. Figure 13 shows the pixel-wise mean and standard deviation of the evaluated FoM values for each of the prompt end times in this scan. We select a prompt end time of 75 ns, as this optimizes the performance at low energy. The optimized energy-dependent FoM for all pixels in the SiPM-based array is shown in Figure 14a. We report the mean and standard deviation of the FoM across all pixels in the detector in Figure 14b.

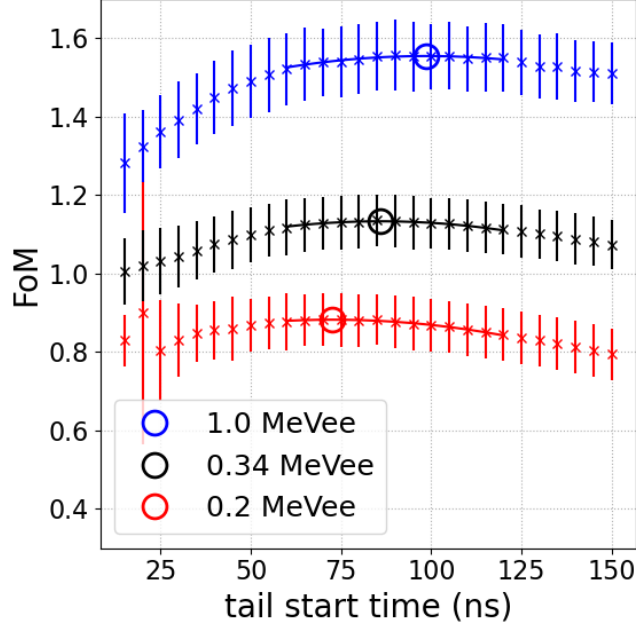


Figure 13. Measurements of the FoM as a function prompt end time in the SiPM-based array. In this figure, red indicates low-energy measurements (0.2 MeVee), black indicates measurements at 0.34 MeVee, and blue indicates measurements at 1 MeVee. The “x” markers show measurements obtained for the given tail-start time in ns. The error bars indicate the standard deviation of the FoM values for the 64 pixels for each prompt end time. The solid line shows a quadratic fit to measurements near the maximum for each energy selection. Finally, the open circle markers indicate the maximum values of the quadratic fits.

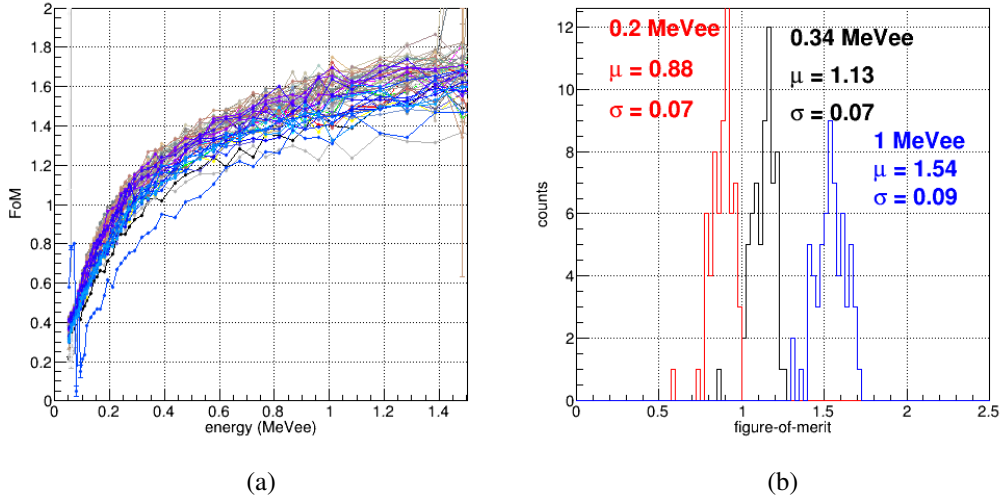


Figure 14. (a) Optimized PSD FoM for all 64 pixels in the SiPM-based detector. The high-noise channel mentioned in Section 2 is apparent in this panel as the trace with the lowest FoM . (b) The projected FoM for all 64 pixels at 0.2 MeVee (red), 0.34 MeVee (black) and 1 MeVee (blue).

4 Neutron Detection Efficiency

The intrinsic neutron efficiency is defined as the ratio of detected neutrons, N_d , to neutrons incident on the detector's face, N_i . To calculate N_i from the ^{252}Cf source over all energies, we start with the source activity, A , measured at some time t after a survey, to determine the current activity:

$$A = A_0 2^{-t/t_{1/2}}, \quad (4.1)$$

where $t_{1/2}$ is the 2.645 year half-life and A_0 is the surveyed activity. The solid angle coverage (Ω) is calculated by summing the solid angles, ω_p of each rectangular pixel, p , assuming a point source:

$$\omega_p = \frac{\mathcal{A} \cos \theta_p}{r_p^2} = \frac{a^2 h}{r_p^3}, \quad (4.2)$$

in which, \mathcal{A} is the area of the face of a pixel, including the inter-pixel gap, a is the pixel pitch, r_p is the distance to the center of the face of pixel p , θ_p is the opening angle from the source to the center of the pixel, and h is the source distance from the detector face. We include the gaps between pixels in this calculation because a neutron that enters the face of the detector through a gap may have a trajectory that brings it into the bulk and may interact with the scintillator. The combined solid angle coverage, Ω , of the detector face is given by:

$$\Omega = \sum_{p=0}^{n-1} \omega_p, \quad (4.3)$$

where n is the total number of pixels. Finally, we account for the 3.09% spontaneous fission branching fraction, B , and the average number of neutrons emitted per fission, $\bar{\nu} = 3.76$ [21]. The total number of incident neutrons expected on the face of the detector for a live time τ (accounting for dead time) is thus

$$N_i = AB\bar{\nu}\tau \frac{\Omega}{4\pi} = A_0 2^{-t/t_{1/2}} \tau B\bar{\nu} \frac{\Omega}{4\pi}, \quad (4.4)$$

We also estimate the ratio of neutrons detected, N_d , per detectable neutron interaction, N_D . We estimate N_D using Geant4[22] simulations of the experimental setup described in Section 2. We use Geant4 version 10.7.4 with the QGSP_BERT_HP physics list. We simulate a number, S , of ^{252}Cf fission neutrons, isotropically emitted from a point source. We then count the number, n_D , of simulated neutrons that undergo at least one elastic scatter with a hydrogen nucleus in the detector volume. The ratio of detectable neutrons per emitted ^{252}Cf neutron is then used to calculate an estimate of N_D :

$$N_D = \left(A_0 2^{-t/t_{1/2}} \tau B\bar{\nu} \right) \frac{n_D}{S}. \quad (4.5)$$

The efficiency for detectable neutrons is intended primarily as a relative measure between the two detectors that controls for geometric effects such as trajectory differences and differences in the gap size between pixels.

To select the detected neutron population, N_d , we use a Bayesian likelihood function constructed from the Gaussian fits to the PSD distribution to calculate gamma and neutron probability metrics, \hat{P}_n and \hat{P}_γ , for each entry in the dataset [23]. Any deposition with a $\hat{P}_n > 99\%$ at any energy is

included in the neutron population, and any deposition with a $\hat{P}_\gamma > 99\%$ at any energy is included in the gamma population. For the PMT-based detector, the probability metric for source $s = \{n, \gamma\}$ is constructed from the product of the individual PMT's contribution to the measurement, indexed by p :

$$\hat{P}_s(E) = \frac{\prod_{p=0}^4 \mathcal{L}_{s,p}(E)}{\prod_{p=0}^4 \mathcal{L}_{n,p}(E) + R \prod_{p=0}^4 \mathcal{L}_{\gamma,p}(E) + \mathcal{L}_O}. \quad (4.6)$$

where $\mathcal{L}_{s,p}(E)$ are peak-normalized distributions taken from the Gaussian fits to the neutron ($s = n$) and gamma ($s = \gamma$) populations and $\mathcal{L}_O = 0.001$ is the likelihood of a third “other” classification. The gamma-to-neutron ratio, R , is given by the number of gammas divided by the number of neutrons. The gamma and neutron numbers used in this ratio are calculated using a first-pass analysis of the dataset as described above, where we take $R = 1$.

For the SiPM-based detector, the probability metrics are taken from the individually measured distributions for each detector pixel, p :

$$\hat{P}_{s,p}(E) = \frac{\mathcal{L}_{s,p}(E)}{\mathcal{L}_{n,p}(E) + R_p(E) \mathcal{L}_{\gamma,p}(E) + \mathcal{L}_O}, \quad (4.7)$$

The energy-dependent gamma-to-neutron ratio for the SiPM-based detector is calculated using the best-fit Gaussian areas:

$$R_p(E) = \frac{A_{\gamma,p}(E) \sigma_{\gamma,p}(E)}{A_{n,p}(E) \sigma_{n,p}(E)} \quad (4.8)$$

Figures 15 and 16 show examples of the neutron selection in various detector pixels in the PMT-based and SiPM-based detectors, respectively. The “total PSD” measure in Figure 15 is equal to the sum of the prompt amplitudes across the four PMTs, divided by the sum of the total amplitudes. This measure is used for visualization only and is not used in the neutron selection. The PSD values in Figure 16 are then used for neutron selection in the given pixel. Additionally, the mean and 1-sigma widths of the gamma and neutron bands for the given pixels are indicated in Figure 16.

In the neutron selection for the PMT-based detector (Figure 15), we find an obvious decrease in neutron population when comparing a central pixel to an edge pixel, and a central pixel to a corner pixel. The SiPM-based populations show much more consistency across pixels. The neutron selection for the worst performing pixel in the SiPM-based detector (pixel number 59) is shown in Figure 16c. This channel had significant excess electronic noise and had the highest trigger threshold setting, which corresponds to an effective neutron threshold of 0.135 MeVee. At higher energies, there is no obvious difference between this channel and others. There is a discrepancy in the apparent endpoints of the spectra shown in Figure 16. This is due to the saturation rejection, which excludes pulses greater than 470 mV in amplitude, combined with variations in light collection.

We show the calibrated energy histograms for each pixel in the PMT-based detector and SiPM-based detector in Figure 17. The effective energy threshold is measured by fitting the following model function to the spectra shown in Figure 17:

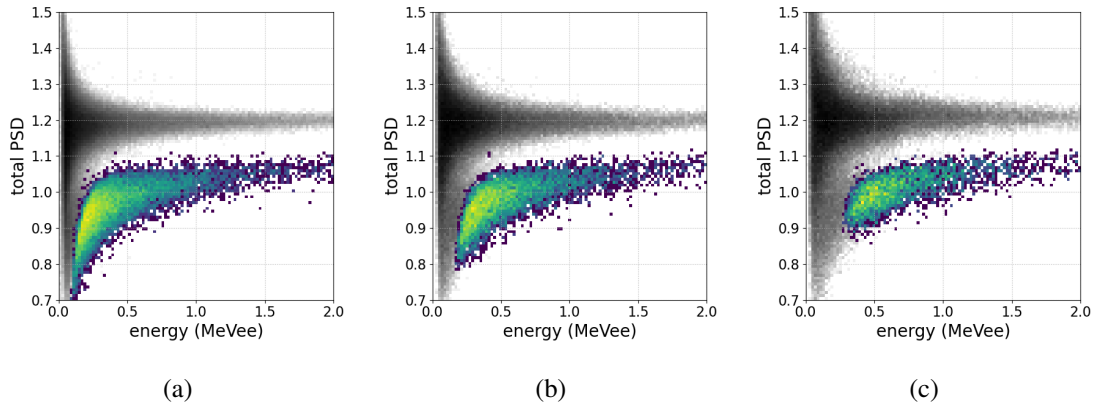


Figure 15. Example neutron selections for pixels in the PMT-based array for a central pixel (a), an edge pixel (b), and a corner pixel (c). The bins in grayscale show events not selected as neutrons, and the blue-green bins indicate selected neutrons.

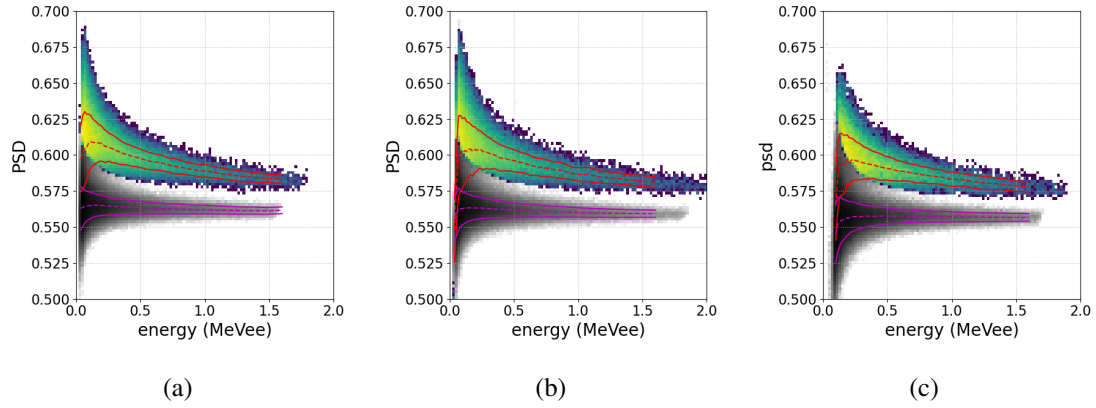


Figure 16. Example neutron selections for pixels in the SiPM-based array for a central pixel (left), a corner pixel (center), and a pixel with excess electronic noise (right). The bins in grayscale show events not selected as neutrons, and the blue-green bins indicate selected neutrons. The mean (dashed lines) and 1-sigma widths (solid lines) of the gamma (magenta) and neutron (red) bands for the given pixels are indicated.

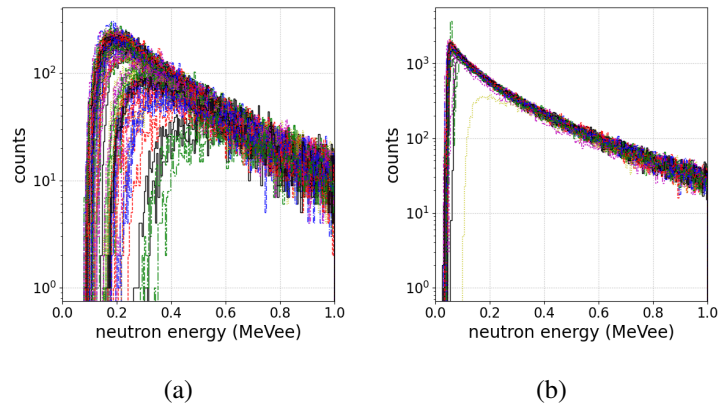


Figure 17. Energy spectra for selected neutron pulses for each pixel in the PMT-based detector (left) and SiPM-based detector (right). Each line represents the histogram for a different pixel.

$$f(x) = a \frac{1}{2} [\text{erf}((x - x_0)/b) + 1] \exp(-(x - x_0)/c) \quad (4.9)$$

where x_0 , a , b , and c are fitting parameters. We take x_0 to be equal to the effective energy threshold for neutrons. The other fitting parameters are not used in any further analysis. The histograms of these effective energy thresholds are shown in Figure 18. We find that the median threshold for the PMT-based array is 0.16 MeVee, spreading all the way up to 0.45 MeVee, while the median threshold for the SiPM-based array is 0.047 MeVee with only a single pixel being higher than 0.1 MeVee. As seen in Figure 17, the neutron recoil energy spectrum is highly peaked toward low energy, so the reduced neutron threshold in the SiPM-based array will have a large effect on the neutron detection efficiency.

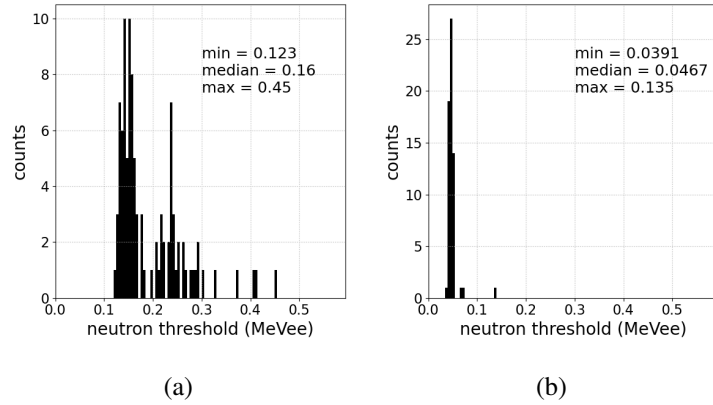


Figure 18. Effective energy threshold for neutron events for all pixels in the PMT-based array (left) and the SiPM-based array (right).

Table 1 contains values for the ^{252}Cf experimental setup required for calculation of N_i in Equation 4.4. The live time, τ , is equal to the run time, t_{run} , minus the dead time, t_{dead} . The dead time for the PMT-based detector is given by the number of events in the dataset before neutron selection, N_{total} , times trigger hold-off period of 2048 ns:

$$t_{dead}(\text{PMT-based}) = N_{total} \cdot (2048\text{ns}), \quad (4.10)$$

The dead time for the SiPM-based detector varies pixel-to-pixel, so we estimate an average value with a term for dead time in the same pixel due to the trigger hold off time of 1024 ns and a term for dead time in all other pixels due to the coincidence rejection:

$$t_{dead}(\text{SiPM-based}) = \frac{1}{64} \cdot N_{total}(1024\text{ns}) + \frac{63}{64} \cdot N_{total}(50\text{ns}). \quad (4.11)$$

Detector	$h \pm \sigma$ (cm)	Ω (sr)	A (μCi)	t_{run} (s)	t_{dead} (s)
PMT-based	142 ± 1	0.005764	154.8	21600.0	37.5
SiPM-based	40 ± 1	0.01603	155.0	14400.0	1.7

Table 1. Table of values for the ^{252}Cf experimental setup required for calculation of N_i in Equation 4.4. The live time, τ , is equal to the run time, t_{run} , minus the dead time, t_{dead} .

Table 2 contains the results for the intrinsic neutron detection efficiency measurement for both the PMT-based detector and the SiPM-based detector. The value of N_d is the number of neutron events for which the calculated neutron probability is $>99\%$. The statistical uncertainty is taken to be $\sqrt{N_d}$. For the PMT-based detector, we estimate the systematic error on N_d using the fractional deviation about the best-fit line in Figure 3. For the SiPM-based detector, we estimate the systematic error on N_d using:

$$\sigma_{syst} = (N_{p>0.984} - N_{p>0.994})/2, \quad (4.12)$$

where $N_{p>0.984}$ is the number of detected pulses with neutron probability $>98.4\%$, and $N_{p>0.994}$ is the number of detected pulses with neutron probability $>99.4\%$. The values of 98.4% and 99.4% are somewhat arbitrary, but are motivated by the uncertainty in the low-energy PSD *FoM* of the SiPM-based detector shown in Figure 14. The cumulative distribution function (CDF) for a standard normal random variable is equal to 99% at a value of $X_{0.99} = 2.327$. This is roughly analogous to the distance in normalized PSD space a pulse needs to be from the gamma mean in order to be considered a neutron. The PSD *FoM* is a measure of the distance in PSD space between the neutron and gamma means, so we use the fractional uncertainty in the PSD *FoM* as a measure of how well distances in PSD space are known. We decrease $X_{0.99}$ by the fractional uncertainty in *FoM* and use the adjusted CDF value (98.4%) for the lower bound for our σ_{syst} calculation. Similarly, we then increase $X_{0.99}$ by the fractional uncertainty in PSD *FoM* and use the adjusted CDF value (99.4%) for the upper bound. We quote the uncertainty on N_i due to the source placement error described in Section 2. The intrinsic neutron detection efficiency (N_d/N_i) is reported in Table 2, along with the error propagated from the stated sources.

Detector	$N_d \pm \sigma_{count} \pm \sigma_{syst}$	$N_i \pm \sigma_{syst}$	$N_d/N_i \pm \sigma$
PMT-based	$1112031 \pm 1055 \pm 4645$	6594197 ± 26773	0.169 ± 0.001
SiPM-based	$3678888 \pm 1918 \pm 100618$	12178050 ± 175103	0.302 ± 0.009

Table 2. Table of results for the intrinsic neutron detection efficiency (N_d/N_i).

Table 3 contains the results for the neutron detection efficiency per unique neutron interaction for both the PMT-based detector and the SiPM-based detector. In contrast to the calculated N_i value, the measured value of N_D has uncertainty due to counting. The fractional systematic uncertainty for N_D is calculated in the same way as that of N_i .

Detector	$N_d \pm \sigma_{count} \pm \sigma_{syst}$	$N_D \pm \sigma_{count} \pm \sigma_{syst}$	$N_d/N_D \pm \sigma$
PMT-based	$1112031 \pm 1055 \pm 4645$	$3545600 \pm 7132 \pm 14395$	0.314 ± 0.002
SiPM-based	$3678888 \pm 1918 \pm 100618$	$5628554 \pm 7346 \pm 80931$	0.654 ± 0.020

Table 3. Table of results for the neutron detection efficiency per detectable (N_d/N_D).

In Figures 19 and 20, we break N_d/N_D up into pixel-wise values. We find, as expected, that the efficiency is much more uniform in the SiPM-based array than it is in the PMT-based array.

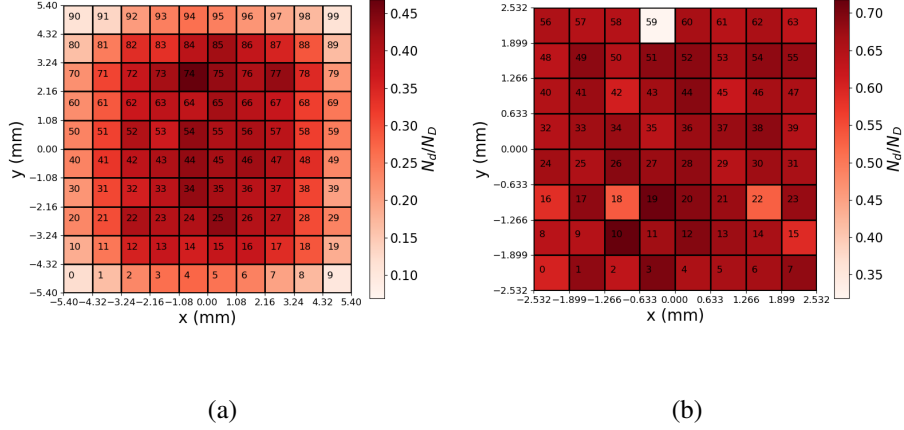


Figure 19. Efficiency maps for the PMT-based detector (left) and for the SiPM-based detector (right). Each grid-square indicates a separate pixel, the index of which is noted in the square. The color scale indicates the value of N_d/N_D for the given pixel. The width of the color scale range for each plot is equal to 0.4, with the upper limit equal to the maximum pixel value for the given detector.

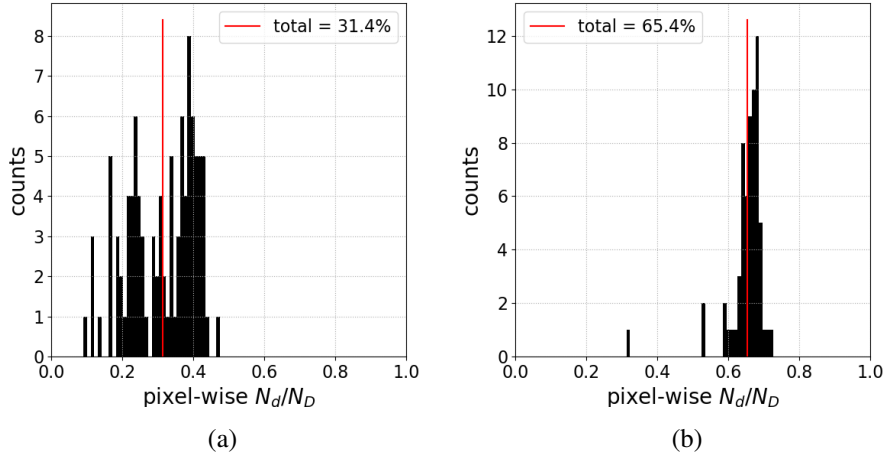


Figure 20. Histograms of the pixel-wise values of N_d/N_D for the PMT-based detector (left) and the SiPM-based detector (right). The vertical red line indicates the efficiency of the entire detector, listed in Table 3.

5 Conclusion

We have examined the intrinsic neutron detection efficiency for both a PMT-based scintillator array using Anger logic readout and a SiPM-based array with 1-to-1 scintillator/photodetector coupling. The use of SiPMs with 1-to-1 coupling greatly improves both the pixel uniformity and the absolute performance of the detector. We find that the intrinsic neutron detection efficiency is $(16.4 \pm 0.2)\%$ for the PMT-based detector, versus $(30.2 \pm 1.7)\%$ for the SiPM based detector. We also report estimated values of neutron detection efficiency per neutron interaction using a Geant4 simulation of the two detectors. We find that the neutron detection efficiency per detectable neutron is 31.4

$\pm 0.5\%$ for the PMT-based array, versus $(65.4 \pm 3.7)\%$ for the SiPM-based array. This means that for the same mass of detector material, a SiPM-based pixelated readout would detect 2.1 times the number of neutrons as a PMT-based detector that uses Anger logic.

If the existing detectors were located at the same distance from a neutron source, the SiPM-based detector would be expected to detect about 40% of the neutrons that the PMT-based detector despite only having about 20% of the active volume. A 2x2 set of SiPM-based detectors would have nearly identical coverage as a single PMT-based detector, and might be used as a drop-in replacement. The resulting combined detector array would have 60% finer pixelation than the PMT-based detector and about 60% higher absolute efficiency.

6 Acknowledgments

The authors would like to thank Steven Hammon from Sandia National Laboratories, who performed the layout of the 64 channel SOUT readout board and Kyle Weinfurther, also of Sandia National Laboratories, for performing an independent review of this publication. We would also like to thank Matthew Blackston, Paul Hausladen, and Jason Newby for their prior work in design and algorithm development for the PMT-based detector. Paul Hausladen also worked with with Agile Technologies to provide the SiPM-based scintillator array. Paul Hausladen and Jason Newby are with Oak Ridge National Laboratory, and Matthew Blackston was formerly with Oak Ridge National Laboratory.

Finally, we thank the US DOE National Nuclear Security Administration, Office of Defense Nuclear Nonproliferation Research and Development for funding this work. Sandia National Laboratories is a multimission laboratory managed and operated by National Technology and Engineering Solutions of Sandia, LLC, a wholly owned subsidiary of Honeywell International, Inc., for the U.S. Department of Energy's National Nuclear Security Administration under contract DE-NA0003525. This paper describes objective technical results and analysis. Any subjective views or opinions that might be expressed in the paper do not necessarily represent the views of the U.S. Department of Energy or the United States Government. Document Release Number SAND2023-092260.

References

- [1] H. O. Anger. *Review of Scientific Instruments* **29** (1958) 27-33
- [2] R. J. Newby, P.A. Hausladen, M. A. Blackston, J. F. Liang. *ORNL/TM-2013/82*:
<https://doi.org/10.2172/1128961>
- [3] G. Zappalà *et al.* *Journal of Instrumentation* **11** (2016) P08014
- [4] K. Nakamura *et al.* *Nucl. Inst. and Meth. in Phys. Res. A.* **623** (2010) 276-278
- [5] G. Romeo *et al.* *Nucl. Inst. and Meth. in Phys. Res. A.* **826** (2016) 31-38
- [6] Zhixiang Zhao *et al.* *IEEE Trans. Nucl. Sci.* **64** (2) (2017) 820
- [7] Zhixiang Zhao *et al.* *IEEE Trans. Nucl. Sci.* **68** (9) (2019) 3200
- [8] Jiajun Zheng *et al.* *IEEE Trans. Nucl. Sci.* **64** (6) (2017) 1401

- [9] J. Newby, P. Hausladen, and M.A Blackston. "Position-Sensitive Organic Scintillators for Nuclear Material Accountancy" *Symposium on International Safeguards: Linking Strategy, Implementation and People* (2014) <https://www.osti.gov/servlets/purl/1163163>
- [10] Nathan P. Giha *IEEE Nucl. Sci. Symp. Atlanta, Ga.* DOI: 10.1109/NSSMIC.2017.8532622 (2015)
- [11] "DT5730/DT5725 User Manual, Rev. 8" *CAEN S.p.A.* (2023)
- [12] "User Manual UM5960 CoMPASS Multiparametric DAQ Software for Physics Applications, Rev. 20" *CAEN S.p.A.* (2020)
- [13] "V1730/VX1730 & V1725/VX1725 User Manual, Rev. 7" *CAEN S.p.A.* (2023)
- [14] R. Brun and F. Rademakers. *Nucl. Inst. and Meth. in Phys. Res. A* **389** (1997) 81-86
- [15] C. R. Harris *et al. Nature* **585 (7825)** (2020) 357-362
- [16] P. Virtanen *et al. Nature Methods* **17** (2020) 261-272
- [17] J. D. Hunter *Computing in Science & Engineering* **9 (3)** (2007) 90-95
- [18] J. Pivarski *et al.* "Uproot v5.0.11" *Zenodo* (2023) <https://doi.org/10.5281/zenodo.8239801>
- [19] H. Klein and S. Neumann. *Nucl. Inst. and Meth. in Phys. Res. A.* **476** (2002) 132-142
- [20] M. Sweany *et al. Nucl. Inst. and Meth. in Phys. Res. A* **927** (2019) 451-462
- [21] S. Croft, A. Favalli, and R. D. McElroy Jr. *Nucl. Inst. and Meth. in Phys. Res. A* **954** (2020) 161605
- [22] J. Allison *et al.* "Geant4 developments and applications" *IEEE Transactions on Nuclear Science* **53** (2006) 270-278
- [23] J. Brennan, E. Brubaker, M. Gerling, P. Marleau, M. Monterial, A. Nowack, P. Schuster, B. Sturm, M. Sweany. *Nucl. Inst. and Meth. in Phys. Res. A* **877** (2018) 375-383